Supplementary Materials and Methods

Genotyping of EAAC1 KO mice

EAAC1 -/- (KO) mice (Memorec Stoffel; Cologne, Germany) were generated by targeted disruption of exon 1 with a neomycin-resistant cassette (Peghini et al., 1997). Heterozygous mice from the 4^{th}-7^{th} backcrossing generation with C57BL/6 WT mice (Harlan, Indianapolis, IN) were used to generate matched WT and KO littermates (P14-21), identified by PCR analysis of tail DNA (Fig. S1*A*). Samples were digested at 50 °C for 2 h-overnight in lysis buffer containing (mM): Tris pH 8.0 (100), EDTA (5), NaCl (200), 0.2% SDS, 1:100 10 μg/μl Proteinase K. DNA samples were diluted 1:1000 and processed for PCR with ready-to-go PCR beads (GE Healthcare, Piscataway, NJ). The PCR primers were chosen to yield a 360 bp fragment for WT (5' AGA AGC TCC TCG GTG GGA CAC 3'; 5' GAG AGC AGC AGC CAG TGA TTC 3') and a 680 bp fragment for the mutant (5' CTG TGC TCG ACG TTC TCA CTG 3'). The PCR protocol included an initial denaturation at 95 °C for 3 min and 34 cycles with denaturation at 95 °C for 30 s, annealing at 63 °C for 30 s, elongation at 72 °C for 90 s.

Western blot

WT and KO littermates (P14-21) were deeply anaesthetized with isoflurane and decapitated in accordance with the guidelines of National Institute of Neurological Disorders and Stroke Animal Care and Use. Hippocampus, cortex and cerebellum samples were homogenized at 4°C for 30 s in a homogenization buffer containing (mM): PMSF (1), EDTA (1) and protease inhibitors (complete tablets, Roche, Germany) in TBS, solubilized in this buffer (with 1% Triton X-100 added) on ice for 40 min with frequent vortexing. Non-solubilized particles were sedimented by centrifugation (20,000 g, 4°C) for 30 min. The supernatant was transferred to a new tube for measuring the total protein concentration. The protein concentration was determined by BCA protein assay (Pierce Chemical, Rockford, IL). Equal amounts of total proteins from WT and KO

littermates (25 μg) were loaded on 4-12% Nupage Novex Bis-Tris gels (Invitrogen, Carlsbad, CA) and then transferred to nitrocellulose membranes (Invitrogen, Carlsbad, CA). Membranes were blocked at RT for 1 h in 10% non-fat milk in TBS with 0.1% Tween-20 (TBST) and probed with the following primary antibodies at 4 °C overnight in 2% non-fat milk-TBST: polyclonal sheep anti-EAAC1-C510B (1:600; Dr. N.C.Danbolt, University of Oslo, Norway), polyclonal guinea pig anti-GLAST:aa524-543 (1:3000; Chemicon, Billerica, MA), polyclonal guinea pig anti-GLT-1:aa554-573 (1:2000; Chemicon, Billerica, MA), polyclonal rabbit anti-EAAT4 and anti-EAAT5 (1:2000; ADI, San Antonio, TX), monoclonal rabbit anti-NR2A clone A12W (1:2000; Upstate, Lake Placid, NY), polyclonal rabbit anti-NR2B (1:2000; Sigma, St. Louis, MO), monoclonal mouse anti-β-tubulin (1:3000; Sigma, St. Louis, MO), monoclonal mouse anti-β-actin (1:3000; Sigma, St. Louis, MO). After washing with TBST 3 times for 5 min, membranes were incubated with 2% non-fat milk-TBST at RT for 2 h with the following horseradish peroxidase-conjugated secondary antibodies (IgG-HRP): rabbit anti-sheep (1:1000; Santa Cruz Biotechnology, Santa Cruz, CA), goat anti-guinea pig (1:2000; Santa Cruz Biotechnology, Santa Cruz, CA), goat anti-rabbit (1:2000; ADI, San Antonio, TX) or sheep anti-mouse (1:2000; Chemicon, Billerica, CA). Following washing with TBST 3 times (15 min each), enhancing chemiluminescent reagents (ECL, Pierce Chemical, Rockford, IL) were used to visualize proteins. For detection with different antibodies, blots were stripped in a solution of (mM) Tris-HCl (62.5) pH 7.5, dithiothreitol (20) 1% SDS at 50 °C for 20 min with agitation and washed with TBST 3 times at RT (10 min each).

For semi-quantitative analysis, protein bands detected by ECL were scanned into Adobe Photoshop (Adobe Systems, San Jose, CA) and images were analyzed with imaging software Gel-Pro 4.5 (Media Cybernetics, Silver Spring, MD). The normalized percentage of detected proteins from KO mice was calculated using standard curves and expressed as relative to that of WT littermates.

Western blot analysis detected no EAAC1 protein in KO mice, whereas expression levels of glutamate transporters GLAST and GLT-1 were similar to those in WT mice in hippocampus, cortex and cerebellum (Fig. S1*C,D*). No protein for the neuronal glutamate transporters EAAT4 and EAAT5 were detected in the hippocampus although, in agreement with previous reports

(Danbolt, 2001), they were present in cerebellum and retina samples, respectively (Fig. S1*C*). These results suggest that no ectopic expression of EAAT4/5 occurs in the hippocampus following genetic disruption of the EAAC1 gene.

The sensitivity of this technique was determined by measuring the absolute band intensity for GLAST and GLT-1 with different protein loads (0-30 μg, in 5 μg steps). The relative band intensities for GLAST and GLT-1 (vs. β-Actin), normalized by those obtained with 25 μg loads that we used for all other Western blot analysis, increased linearly with the amount of protein load (data not shown). The intercepts of the unity line with the upper and lower 99% confidence bands were projected on the x-axis, which reported the protein loads. One half of the difference between these two points was taken as a measure of the sensitivity of Western blot analysis for GLAST and GLT-1 in WT and KO mice (GLAST: WT 0.11, KO 0.10; GLT-1: WT 0.20, KO 0.14).

Immunohistochemistry

WT and KO littermates (P14-21) were deeply anaesthetized with ketamine injection (1:10^5 v/w), trans-cardially perfused with PBS for 10 min and then with 4% paraformaldehyde (PFA) in phosphate buffer (0.1 M; PB-4% PFA) for 15 min. Dissected hippocampi were post-fixed in PB-4% PFA at RT for 2 h, rinsed with PBS and cryo-protected in PB-30% sucrose at 4 °C overnight. Cryostat sections (16 μm thick) were collected on slides and double-labeled with monoclonal mouse anti-neuronal nuclei (Neu-N, 1:500; Chemicon, Billerica, CA) plus one of the primary antibodies previously described for Western blot analysis: anti-EAAC1-C510B (1:500), anti-GLAST (1:500), anti-GLT-1 (1:250) in PBS containing: 2% BSA, 0.3% Triton X-100, 0.1% sodium azide, at RT overnight. Slides were washed for 3 times (5 min each) with PBS and incubated for 2 h with the following secondary antibodies: donkey anti-mouse Cy3 (1:600; Molecular Probes, Eugene, OR), donkey anti-sheep Alexa Fluor 488 (1:500; Molecular Probes, Eugene, OR), goat anti-mouse Alexa Fluor 594 (1:600; Molecular Probes, Eugene, OR), goat anti-guinea pig Alexa Fluor 488 (1:500; Molecular Probes, Eugene, OR). Slides were mounted with Vectashield mounting medium (Vector Labs, Burlingame, CA). Immunoreactivity was visualized and acquired

with a confocal laser scanning microscope (Zeiss LSM 510, Thornwood, NY) using 10X and 40X/oil objectives. The selected images were cropped and aligned in Adobe Photoshop 7.0 (San Jose, CA) or ImageJ.

Immunohistochemical staining of hippocampal slices showed that gross anatomical architecture was preserved in KO mice, but EAAC1 protein was absent (Fig. S1*B*). The expression pattern of glial transporters GLAST and GLT-1 was indistinguishable in WT and KO mice (Fig. S1*B*).

Immunostaining for HNE was performed on hippocampal slices from P14-21 or 8 week old mice (250 μm thick) prepared as described in the Electrophysiology section. Slices were fixed 1 h and 3 h after preparation and storage in low $CaCl_2$-high $MgCl_2$ ACSF, or after an additional 30 min incubation in ACSF added with H_2O_2 (200 μM), in PBS-4% PFA at 4 °C overnight. Slices were kept in PBS-30% sucrose until cryostat sections were prepared (16 μm thick). The primary rabbit antiserum anti-HNE (1:200) was obtained from ADI (San Antonio, TX). Donkey anti-rabbit Alexa Fluor 488 (1:500; Molecular Probes, Eugene, OR) was used as a secondary antibody.

Electron microscopy

Acute hippocampal slices (300 μm thick, from 3 WT and 3 KO littermates) processed for EM analysis were prepared as for the electrophysiological experiments. Slices were fixed at RT for 1 h with 2% glutaraldehyde, 2% PFA in 0.1 N cacodylate buffer and then stored at 4 °C overnight in the same fixative. After 3 washes in 0.1 N cacodylate buffer, the CA1 region was cut in two halves, perpendicularly to the pyramidal cell layer. These samples were treated with 1% osmium tetroxide for 1 hr on ice, en bloc mordanted with 0.25% uranyl acetate at 4 °C overnight, washed and dehydrated with a graded series of ethanol and finally embedded in epoxy resins. Thin sections (70-90 nm) were cut along the arborization of the dendrites in of *stratum radiatum*, counterstained with lead citrate and uranyl acetate and examined on a JEOL 1200 EX transmission electron microscope. A subset of slices was also obtained from 3 pairs of WT and KO littermates, deeply anaesthetized with halothane and transcardially perfused with 30 ml of 2%

glutaraldehyde, 2% PFA in 0.1 N cacodylate buffer. Brains were stored in this fixative at RT for 1 h and at 4 °C overnight. Slices were cut at 100 μm with a vibratome (VT1000S, Leica, Germany) and processed as previously described.

Images were collected with a CCD digital camera system (XR-100 from AMT, Danvers, MA). We analyzed the innermost region of these sections, being the least damaged by the vibratome cut. Images were taken from regions located ~100 μm away from the pyramidal cell layer, in *stratum radiatum*. Twenty adjacent frames (4 μm x 4 μm; 12000X) were acquired and ten consecutive ones were used for the analysis. A binary mask of these images was manually drawn using a tablet computer and the ECS fraction was calculated as the area fraction with black pixels using the software ImageJ.

Two-photon imaging of biocytin-filled neurons

CA1 pyramidal neurons were patched in the whole-cell configuration for at least 30 min using the following solution (mM): KCH_3SO_3 (120), EGTA (10), HEPES (20), MgATP (2), NaGTP (0.2), QX-314Br (5), 290 mOsm, pH 7.2 added with biocytin 0.4%. Slices were fixed in PBS 4% PFA at 4 °C overnight and then transferred to PBS. After permeabilization with 0.1% Triton X-100, slices were incubated in 0.1% streptavidin-Alexa 488 conjugate at RT for 2 h, mounted with Vectashield antifading medium and imaged under 2-photon illumination (LSM510 microscope; Zeiss, Thornwood, NY). Image stacks (0.1-1 μm steps) were analyzed off-line with the ImageJ software to monitor spine density and size.

Diffusion measurements using integrative optical imaging

Using previously described methods (Thorne and Nicholson, 2006), we imaged the diffusion of Texas red dextrans (3, 10, 40 and 70 KDa, TRdx3, TRdx10, TRdx40 and TRdx70, respectively) and red-fluorescent quantum dot nanocrystals (QD655) pressure applied (200 ms x 5 PSI) in free solution and in *stratum radiatum* of hippocampal slices using a glass pipette (1.5-

2.5 MΩ) connected to a Picospritzer III (Parker Hannifin Corporation General Valve Division, Fairfield, NJ). An area of 720 x 540 μm was imaged using a Zeiss Achroplan 10X water-immersion objective (0.5 NA) with a 0.4 magnification. Illumination was provided by a 100 W halogen epifluorescence lamp (AttoArc HBO), controlled by a Uniblitz shutter and driver (Rochester, NY). The projection of the 3D cloud of diffusing probe on the 2D image plane of a CCD camera (N50, Hamamatsu Photonics, Bridgewater, NJ; 640 x 480 pixels) was described by

$$I_i\,(r,\gamma_i) = \mathrm{A}_i\, e^{-\left(\frac{r}{\gamma_i}\right)^2}$$

and

$$\gamma_i^2 = 4\,D^*\left(t_i + t_0\right),$$

where I_i = fluorescence intensity of the *i*th image at radial distance r from the source, A_i = an expression that incorporates the defocused point spread function of the microscope, t_0 = time offset from the time of the puff application t_i. The first expression was used to fit the concentration distributions at time t_1, t_2…t_n (Levenberg-Marquardt algorithm, IgorPro) to derive γ_I (the width of the Gaussian function). The diffusion coefficient D was estimated from the linear regression of $\gamma^2/4$ upon t_i. The signal of the background image was subtracted from that of the images taken after the puff. To avoid thermal convection currents, we measured D in free solution at RT (24 °C) and corrected it by Q_{10} = 1.3 for comparison with D* obtained in slices (34 °C). In these experiments λ (i.e. the tortuosity value of each probe) was measured as:

$$\lambda = \sqrt{\left(\frac{D}{D^*}\right)}$$

The hydrodynamic diameter of different molecules (d_H) was calculated from the Stokes-Einstein equation:

$$d_H = \frac{KT}{3\pi\eta D}$$

where K = Boltzmann's constant ($1.38 \cdot 10^{-23}$ J/K), T = temperature in °K (307), η = viscosity of water at 307 °K ($7.35 \cdot 10^{-4}$ Pa · s) and D = diffusion coefficient of each probe.

To calculate the average width of the ECS (d_{ECS}), we assumed a parallel plane geometry (Thorne and Nicholson, 2006) and fitted our results with the equation:

$$\lambda = \lambda_{\theta=0}\left[(1-\theta)\left(1-1.004\theta+0.418\theta^3+0.21\theta^4-0.169\theta^5\right)\right]^{-\frac{1}{2}}$$

where $\lambda_{\theta=0}$ is λ for a vanishingly small molecule and $\theta = d_H/d_{ECS}$.

Diffusion measurements using two-photon microscopy

We used this technique to have a more accurate estimate of the diffusion of small molecules like Alexa Fluor 350, whose molecular weight (349.29 Da) is close to that of glutamate (147 Da) (Savtchenko and Rusakov, 2005; Zheng et al., 2008). The advantage of this method, as pointed out by (Savtchenko and Rusakov, 2005), lies in the ability of two-photon excitation to be confined to a thin focal plane (~1 μm in z-axis), much wider than the ECS and much thinner than the scanned area (~230 μm). The recorded profiles provide information about the concentration profile of the indicator in space and time. We filled a patch pipette (1.5-2 MΩ) with the cell-impermeable indicator Alexa Fluor 350 (Invitrogen, Carlsbad, CA) dissolved to 0.2 mM in ACSF. The pipette was connected to a Picospritzer III (Parker Hannifin Corporation General Valve Division, Fairfield, NJ). We used pressure applications of 5-10 ms X 13 PSI to eject the fluorescent indicator in free medium or hippocampal slices from WT and KO mice (~ 40 μm from the slice surface). The puff was triggered 200 ms after the beginning of the image acquisition. We used an imaging microscope (Zeiss LSM 510, Thornwood, NY) powered by a Ti:sapphire pulsed laser (Coherent Inc., Santa Clara, CA) tuned to 760 nm, with an average beam power under the 40X objective of ~10 mW. A line scan (521 Hz) was performed orthogonally to the pipette at the focal plane of the tip, 5-10 μm away from it. Ten consecutive line scans (5.76 s) were performed with each pipette, every 30-60 s. They were stored as 8-bit images, preserving the original brightness values. The analysis was performed on the average of these 10 images. We measured the light intensity profiles before the puff and then every 100 ms, 200 ms-1 s after the

puff. Each fluorescence profile was fitted with a Gaussian function (Levenberg-Marquardt algorithm, IgorPro). The pre-puff fluorescence profile was routinely subtracted from the other recorded diffusion profiles to avoid any bias from residual fluorescence in between puffs. Within the selected time window, the linearity of diffusion of a molecule (Alexa Fluor 350) from a point source (the pipette) was verified and D was estimated from the linear regression of $\gamma_i^2/4$ versus time. This set of experiments was performed at room temperature (24 °C).

Supplementary Figure Legends

Supplementary Figure 1. Characterization of EAAC1 KO mice. ***A*** PCR of genomic tail DNA from WT, heterozygous (Het) and KO littermates. The DNA fragment corresponding to EAAC1 (360 bp) is evident in WT and Het mice, whereas that corresponding to the neomycin cassette (Neo, 680 bp) is detected in Het and KO mice. In addition, these mice show a band corresponding to the EAAC1 gene inserted with the Neo cassette (1520 bp). ***B*** Immunohistochemical staining of hippocampal slices for EAAC1 (top row), GLAST (middle row), GLT-1 (bottom row) (all shown in green) and the nuclear marker Neu-N (red), in WT and KO mice. Panels on the right are close-up views of the white-boxed regions in left panels. EAAC1 is undetected in KO mice. ***C*** Western blots for EAAC1, GLAST, GLT-1, EAAT4, EAAT5 from Hippocampus (hippoc), cortex (Ctx), cerebellum (Cb) and retina (Ret) of WT and KO littermates. Positive control: β-tubulin. ***D*** Summary of semi-quantitative analysis of Western blot band intensities in WT and KO mice. Left: WT-normalized band intensities for EAAC1, GLAST and GLT-1 in KO mice hippocampus (EAAC1 ***p = 4.2E-7, n = 5; GLAST p = 0.24, Power = 0.34, n = 6; GLT-1 p = 0.23, Power = 0.37, n = 5). Center and right: hippocampus-normalized band intensities for GLAST (center) and GLT-1 (right) in cortex and cerebellum. The cerebellum has more GLAST and less GLT-1 protein in respect to the hippocampus (center: WT Ctx p = 0.82; KO Ctx p = 0.46; WT CB *p = 0.04; KO CB *p = 0.02, n = 6; right: WT Ctx p = 0.07; KO Ctx *p = 0.02; WT CB ***p = 0.0004; KO CB *p = 0.02, n = 5). No significant difference between WT and KO samples is observed (GLAST Ctx WT-KO p = 0.24, Power = 0.10; Cb WT-KO p = 0.92, Power = 0.05; GLT-1 Ctx WT-KO p = 0.34, Power = 0.16; Cb WT-KO p = 0.34, Power = 0.14), even when comparing raw data (GLAST hippoc WT-KO p = 0.11; Ctx WT-KO p = 0.58; Cb WT-KO p = 0.09; GLT-1 hippoc WT-KO p = 0.34; Ctx WT-KO p = 0.51; Cb WT-KO p = 0.18). ***E*** Western blots for NR2A, NR2B from WT and EAAC1 KO hippocampus. Positive control: β-actin. ***F*** Summary of Western blot analysis for NR2A and NR2B. Similar protein amounts are detected in WT and KO samples (NR2A WT-KO p = 0.23, Power = 0.31; NR2B WT-KO p = 0.33, Power = 0.65, n = 3). ***G*** Immunohistochemical staining for HNE in hippocampal slices from WT and KO mice is comparable between 1 h and 3 h of *in vitro*

incubation. The immunoreactivity increases with 30 min treatment with H_2O_2 (200 μM) and is more pronounced in older animals. Each panel represents a close-up view of hippocampal area CA1. The susceptibility to oxidative stress increases with age but is not affected by EAAC1.

Supplementary Figure 2. EAAC1 does not alter the glutamate concentration in the cleft. ***A*** Summary of mEPSC analysis in normal ACSF in WT (white, n = 8) and KO mice (red, n = 4; amplitude p = 0.22, rise time p = 0.65, t_{50} p = 0.53). Insets show representative traces of average mEPSCs in WT and KO slices. ***B*** Summary of mEPSC analysis recorded with 0 mM Mg^{2+} in the extracellular solution in WT (white, n = 11) and KO mice (red, n = 11; amplitude p = 0.59, rise time ***p = 1.8E-5, t_{50} p = 0.79). Insets show representative traces of average mEPSCs in WT and KO slices. ***C*** Pairs of AMPAR EPSCs, 100 ms apart, recorded in WT and KO mice in control, DGG (1 mM) and wash-out. ***D*** Summary of the effect of DGG on AMPAR EPSC amplitude in WT (white, n = 5) and KO mice (red, n = 6, p = 0.72). ***E*** DGG reversibly increases PPR (WT PPR_{Ctrl}-PPR_{DGG} **p = 0.004, PPR_{DGG}-$PPR_{W/O}$ *p = 0.02; KO: PPR_{Ctrl}-PPR_{DGG} **p = 0.007, PPR_{DGG}-$PPR_{W/O}$ **p = 0.001).

Supplementary Figure 3. Quantification and CV analysis of the AMPAR and NMDAR components of composite glutamatergic EPSCs. ***A*** Left: Average EPSCs at different holding potentials. Thick lines highlight initial slope and shaded areas the time window over which $Q_{30\text{-}80}$ was calculated. Right: I/V plots of initial slope and $Q_{30\text{-}80}$ in WT mice (n = 6). ***B*** As in *A*, in KO mice (n = 6). ***C*** CV slope in sensitive to changes in release probability and decreases with paired-pulse facilitation in WT (black, n = 11, **p = 0.007) and KO mice (red, n = 12, ***p = 0.0006; WT–KO CV slope $EPSC_1$ p = 0.28, WT–KO CV slope $EPSC_2$ p = 0.17). ***D*** CV $Q_{30\text{-}80}$ also decreases with paired-pulse facilitation at +50 mV in WT (black, n = 8, *p = 0.036) and KO mice (n = 8, *p = 0.020). ***E*** At -70 mV, CV $Q_{30\text{-}80}$ and CV slope are similar in WT (black, n = 13, **p = 0.003) and KO mice (red, n = 27, ***p = 0.0004; WT–KO $Q_{30\text{-}80}$ p = 0.41, WT–KO CV slope p =

0.74). ***F*** Postsynaptic manipulations the number of available postsynaptic NMDARs (CPP 1 μM) do not unmask any difference in CV $Q_{30\text{-}80}$ between WT (black, n = 18, **p = 0.004) and KO mice (red, n = 9, p = 0.21; WT–KO CV $Q_{30\text{-}80}$ p = 0.60, WT–KO CV $Q_{30\text{-}80}$ CPP p = 0.88).

Supplementary Figure 4. EAAC1 does not change release probability. ***A*** mEPSC recordings in WT and KO mice. Right: mEPSC frequency is similar in WT (n = 9) and KO mice (n = 5; p = 0.56). ***B*** Time course of EPSC amplitude at holding potentials shown in the top axis. AMPAR EPSCs were recorded at -70 mV and then blocked by NBQX (10 μM). NMDAR EPSCs were recorded at +50 mV and then blocked by CPP (10 μM). Insets show examples of single and paired AMPAR and NMDAR EPSCs. In these experiments, the stimulus intensity was set to ~60% of that required to elicit an action current while in the cell-attached configuration (data not shown). ***C*** In whole-cell configuration, the amplitude of AMPAR and NMDAR EPSCs is similar in WT (white, AMPAR EPSCs n = 13, NMDAR EPSCs n = 7) and KO mice (red, AMPAR EPSCs n = 11, p = 0.71; KO NMDAR EPSCs n = 9, p = 0.47). ***D*** AMPAR and NMDAR EPSC PPR is similar in WT (white, AMPAR n = 9, NMDAR n= 7) and KO mice (red, AMPAR EPSCs n = 10, p = 0.13, NMDAR EPSCs n = 9, p = 0.35). ***E*** CV of AMPAR EPSC amplitude decreases with paired-pulse facilitation in WT (white, n = 8, *p = 0.019) and KO mice (red, n = 9, **p = 0.007). ***F*** CV of NMDAR EPSC amplitude decreases with paired-pulse facilitation in WT (white, n = 8, *p = 0.048) and KO mice (red n = 9, *p = 0.038).

Supplementary Figure 5. Ifenprodil does not alter release probability. ***A*** Summarized effect of ifenprodil on NMDAR EPSC amplitude at ±50 mV in WT and KO mice, in the presence of extracellular D-Serine (100 μM) and internal BAPTA (10 mM) ($WT_{+50\ mV}$ *p = 0.014, $WT_{-50\ mV}$ p = 0.66, n = 7 (black circle), $KO_{+50\ mV}$ ***p = 4.7E-6, KO_{-50mV} **p = 0.002, n = 11 (red circle), $WT–KO_{+50mV}$ p = 0.66, $WT–KO_{-50mV}$ *p = 0.019). ***B*** Summarized effect of Ro-25,6981 (0.5 μM): WT_{+50mV} **p = 0.003, WT_{-50mV} p = 0.76, n = 7 (grey circle), KO_{+50mV} ***p = 0.0009, KO_{-50mV} ***p =

0.0002, n = 8 (pink circle), WT–KO_{+50mV} p = 0.43, WT–KO_{-50mV} **p = 0.007). ***C*** Paired AMPAR EPSCs at -70 mV in WT and KO mice, before and after ifenprodil (5 μM). ***D*** As in *C*, in 0 Mg^{2+} and 1 mM MK-801 in the pipette solution. ***E*** Summary of the effects of ifenprodil on EPSC amplitude (WT ACSF (black) n = 5, p = 0.95; WT 0 Mg^{2+} (grey) n = 6, p = 0.66; KO ACSF (red) n = 6, p = 0.86, KO 0 Mg^{2+} (pink) n = 6, p = 0.75). ***F*** Summarized effect of ifenprodil on AMPAR EPSC PPR (WT ACSF (black) n = 5, p = 0.49, KO ACSF (red) n = 6, p = 0.10; WT 0 Mg^{2+} (grey) n = 6, p = 0.09, WT ACSF-0 Mg^{2+} *p = 0.01, KO 0 Mg^{2+} (pink) n = 6, p = 0.09, KO ACSF-0 Mg^{2+} *p = 0.02). ***G*** Correlation between the effect of NR2B antagonists (ifenprodil and Ro-25,6981) on NMDAR EPSC amplitude and t_{50} in WT (black, n = 23) and KO mice (red, n = 29). The r values in the figure represent the Pearson's correlation coefficients. ***H*** Lack of correlation between the effect of CPP (1 μM) on NMDAR EPSC amplitude and t_{50} in WT (black, n = 10) and KO mice (red, n = 7).

Supplementary Figure 6. Ifenprodil rescues LTP in KO mice: an "in-slice" comparison. ***A*** Left: time course of normalized fEPSC slope before and after TBS to path 1, in a WT mouse. Right: in ifenprodil (5 μM), in the same slice, TBS to path 2 elicits similar LTP. Insets show average traces recorded 5-0 min before and 5-10 min and 25-30 min after TBS. ***B*** As in *A*, in a KO mouse. ***C*** Time course of normalized fEPSCs averaged in WT mice (n = 7) in control conditions (left) and in ifenprodil (right). ***D*** Same as in *C*, in KO mice (n = 8). ***E*** Summary of the effect of ifenprodil on LTP in WT (black) and KO mice (red; control **p = 0.003, ifenprodil *p = 0.043). Data in panels (c-e) are displayed as mean ± S.E.M.

Supplementary Figure 7. Analysis and validation of glutamate clearance measurements. ***A*** Schematic diagram of the analytical approach used to derive the time course of glutamate clearance from transporter currents. The time course of glutamate clearance in TBOA is approximated by an exponential function, which once deconvolved from the transporter current enables to estimate the time course of the filter. This is then deconvolved from the control transporter current to derive the time course of the clearance under control conditions. ***B*** The centroid of STCs does not change with paired-pulse facilitation, suggesting that the filter behaves linearly within the range of stimulations used in our experiments (WT (black) n = 8, KO (red) n = 13; PPR $<t>_{STC}$ WT-KO p = 0.65, PPR STC WT-KO p = 0.82). ***C*** Left: comparison between deconvolution-derived and centroid-derived centroids of STC glutamate clearance. Both analytical methods show that the centroid of glutamate clearance derived from STCs is slower in WT (n = 7) than in KO mice (n = 6; deconvolution derived STC $<t>_{clearance}$ WT-KO *p = 0.02, centroid derived STC $<t>_{clearance}$ WT-KO *p = 0.02). However, the estimates from the deconvolution analysis tend to be slower than those obtained from the centroid analysis, presumably because of an underestimate of the filter consequent to the exponential approximation of the TC clearance in TBOA (WT deconvolution derived STC $<t>_{clearance}$-centroid derived STC $<t>_{clearance}$ p = 0.32, KO deconvolution derived STC $<t>_{clearance}$-centroid derived STC $<t>_{clearance}$ *p = 0.02). Right: comparison between deconvolution-derived and centroid-derived centroids of FTC glutamate clearance. Both analytical methods show that the glutamate clearance derived from FTCs is similar in WT and KO mice (deconvolution analysis WT-KO p = 0.61, centroid analysis WT-KO p = 0.29). As for STCs, the estimates obtained from FTCs tend to be slower when using the deconvolution approach (WT deconvolution derived FTC $<t>_{clearance}$-centroid derived $<t>_{clearance}$ p = 0.19, KO deconvolution derived FTC $<t>_{clearance}$-centroid derived $<t>_{clearance}$ **p = 0.003). ***D*** The STC (left) and FTC filters (right) derived from deconvolution analysis are similar in WT and KO mice. ***E*** Left: comparison between deconvolution-derived and centroid-derived STC filters. Both approaches indicate that the STC filter is similar in WT and KO mice (deconvolution derived STC $<t>_{filter}$ WT-KO p = 0.95, centroid derived STC $<t>_{filter}$ WT-KO p = 0.29). However, the filter tends to be faster when using the deconvolution approach (WT

deconvolution derived STC $<t>_{filter}$-centroid derived STC $<t>_{filter}$ p = 0.30, KO deconvolution derived STC $<t>_{filter}$-centroid derived STC $<t>_{filter}$ **p = 0.004). Right: comparison between deconvolution-derived and centroid-derived FTC filters. The filter is similar in WT and KO but tends to be faster with the deconvolution approach (deconvolution derived FTC $<t>_{filter}$ WT-KO p = 0.96, centroid derived FTC $<t>_{filter}$ WT-KO p = 0.22; WT deconvolution derived FTC $<t>_{filter}$-centroid derived FTC $<t>_{filter}$ p = 0.12, KO deconvolution derived FTC $<t>_{filter}$-centroid derived FTC $<t>_{filter}$ ***p = 0.0008).

Supplementary Figure 8. Analysis of the error that the TC fitting procedure introduces on the derived time course of glutamate clearance. ***A*** Left: examples of WT and KO STCs with their corresponding fits (green). Right: Residual currents of experimentally recorded STCs in WT (n = 7) and KO astrocytes (n = 6), normalized by the peak of their corresponding STC (mean ± S.D.). ***B*** Summary analysis of the residual currents in WT and KO slices. ***C*** Top left: examples of an idealized STC (black) and a number of inaccurate fits (rainbow colours). Top right: residual currents obtained by subtracting the idealized STC from the inaccurate fits. Bottom left: filter deconvolved from idealized STC and the bad fits. Bottom right: clearances derived from the deconvolution procedure. ***D***. χ^2 analysis of the residuals of the inaccurate fits displayed as a function of their corresponding mis-estimate of the $<t>_{clearance}$. Our fit of the STC traces would only lead to a 4-5% error in the $<t>_{clearance}$, which is negligible in respect to the WT-KO difference observed in Fig. 1.

Supplementary Figure 9. Analysis of the effects of changing glial transporters' efficiency and of the linearity of TCs. A Top: the four panels show the simulated astrocytic STCs obtained at four different values of ECS width (20-200 nm). All traces represent simulated STCs obtained in

the presence of 10800 μm^{-2} glial transporters and no EAAC1. The efficiency of glial transporters varies from 100% (red), 15% (orange) to 0% (yellow). Middle: summary results of the influence of glial transporters' efficiency on $<t>_{STC}$. Bottom: effect of varying glial transporters' efficiency on perisynaptic NMDAR activation. ***B*** The STC amplitude, but not its time course, changes linearly with the number of glutamate molecules released. Top: example traces of simulated STCs in response to release of various amounts of glutamate. Bottom: analysis of STC amplitude and <t>. ***C*** Simulated STCs in response to trains of glutamate release events (2000 molecules each). The amplitude and <t> of the second STC are indistinguishable from that of the first STC for a range of inter-pulse intervals (IPI).

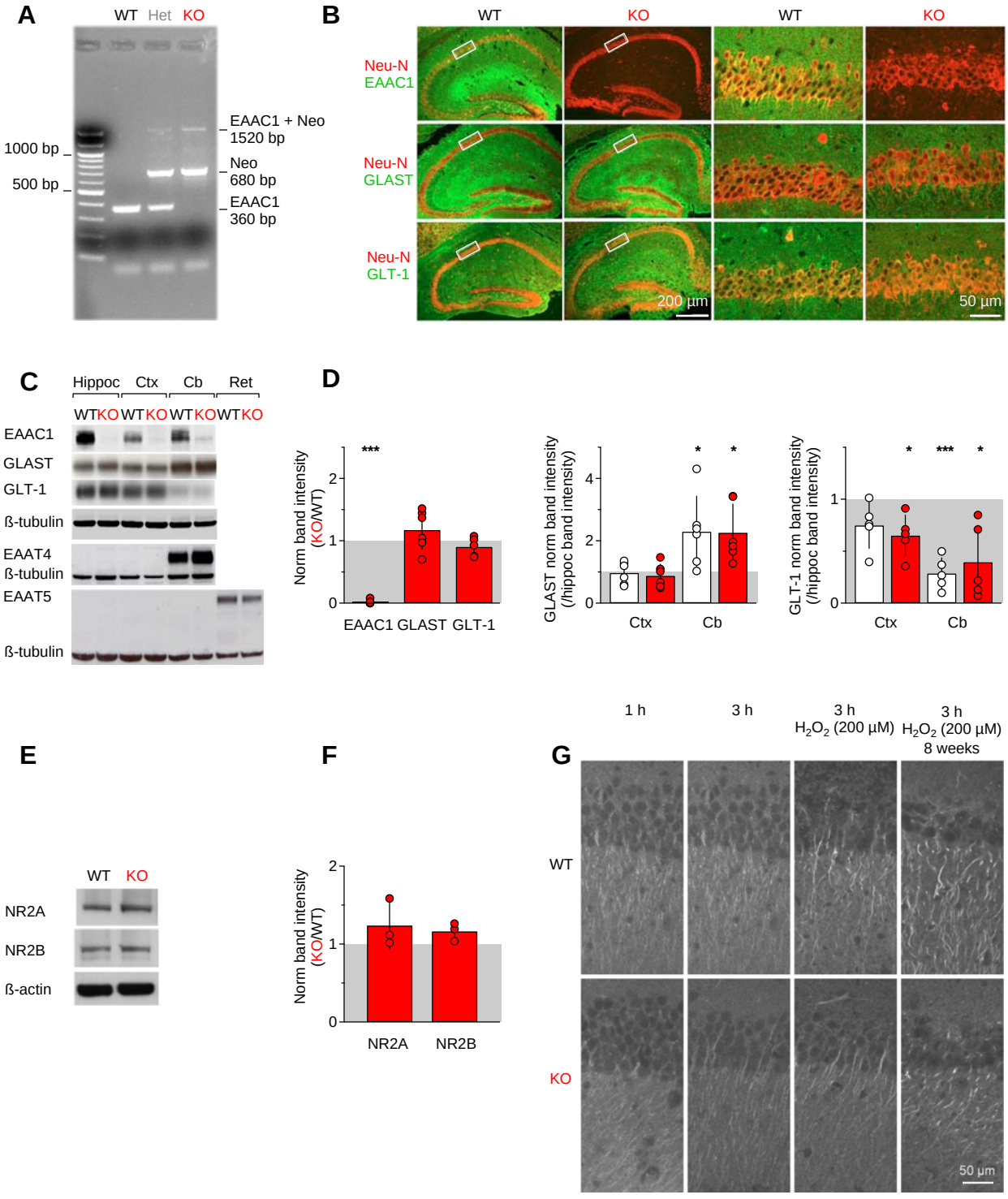

Supplementary Figure 1

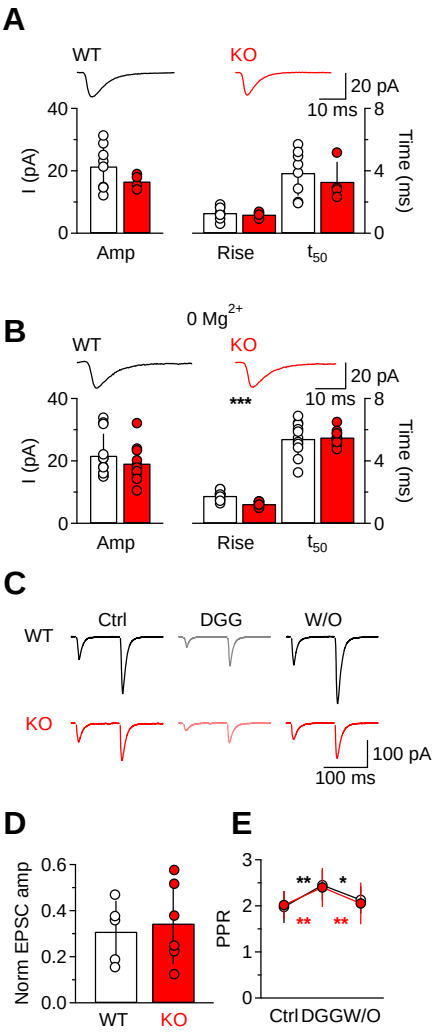

Supplementary Figure 2

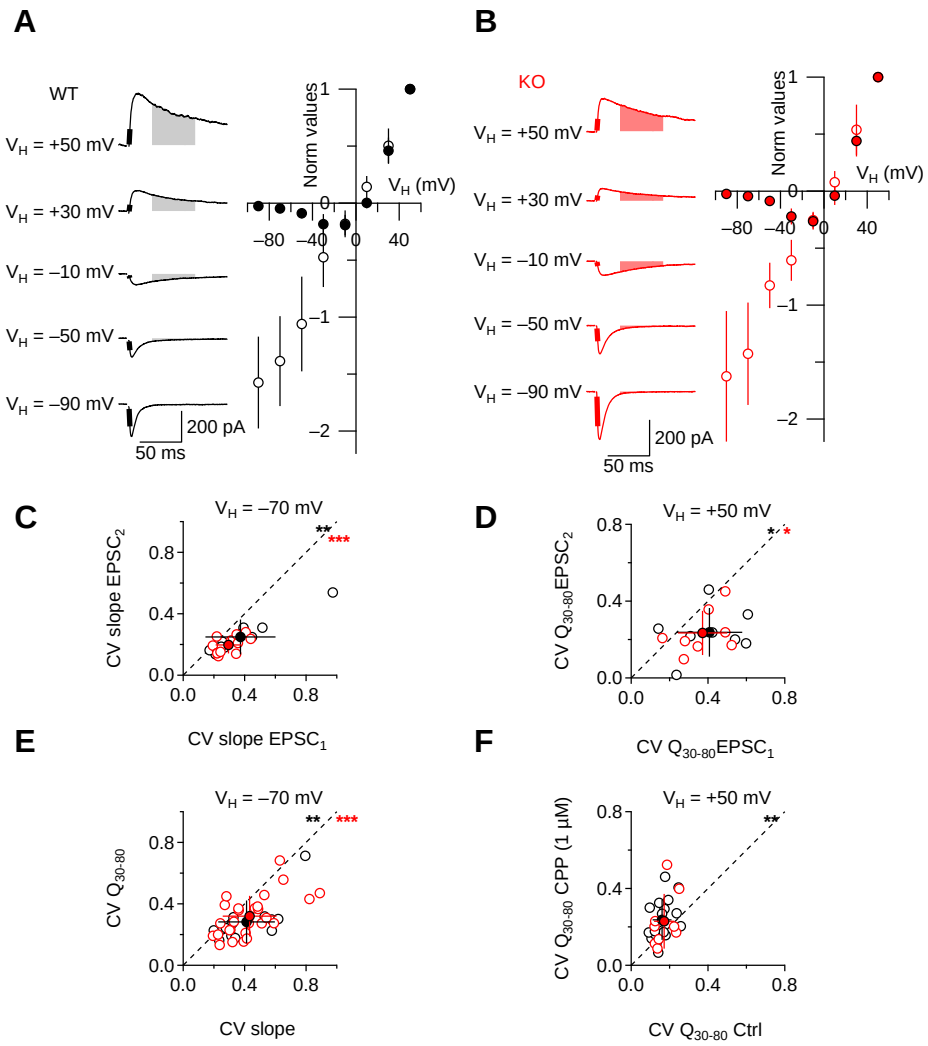

Supplementary Figure 3

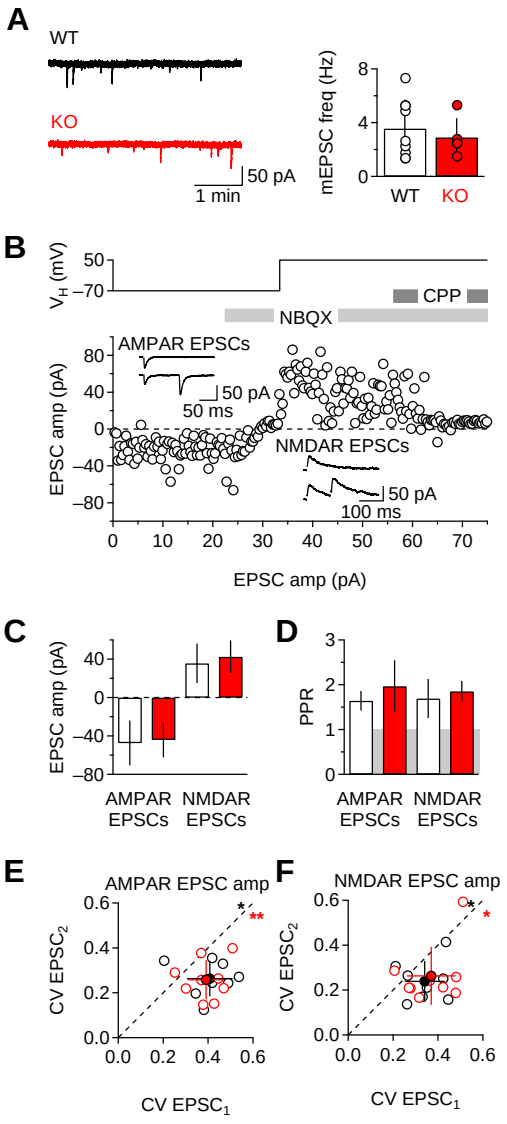

Supplementary Figure 4

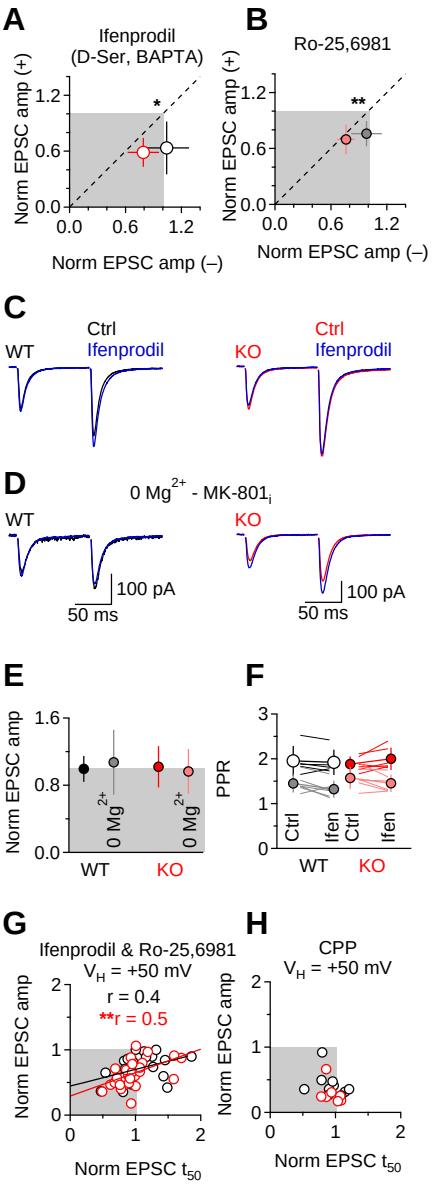

Supplementary Figure 5

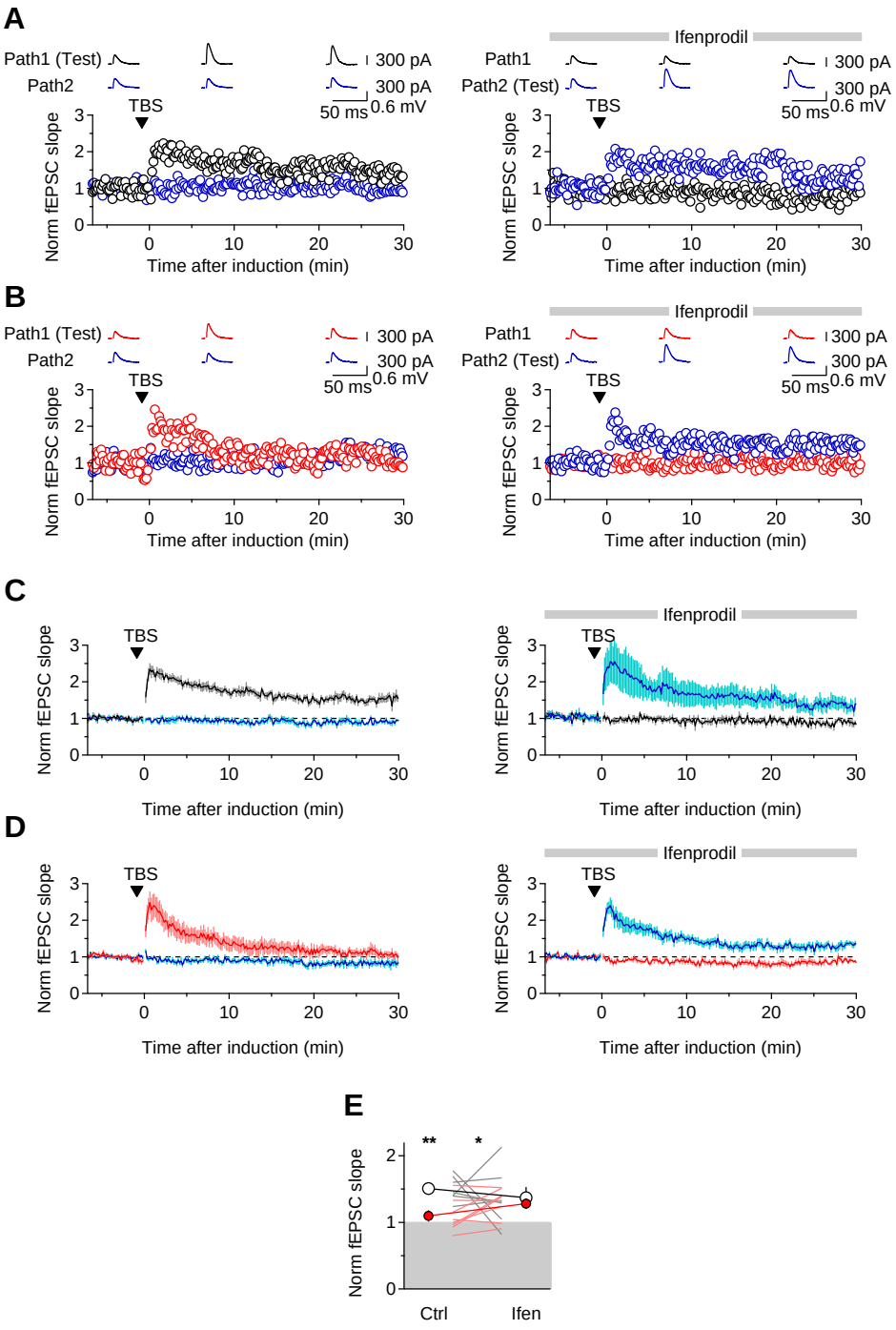

Supplementary Figure 6

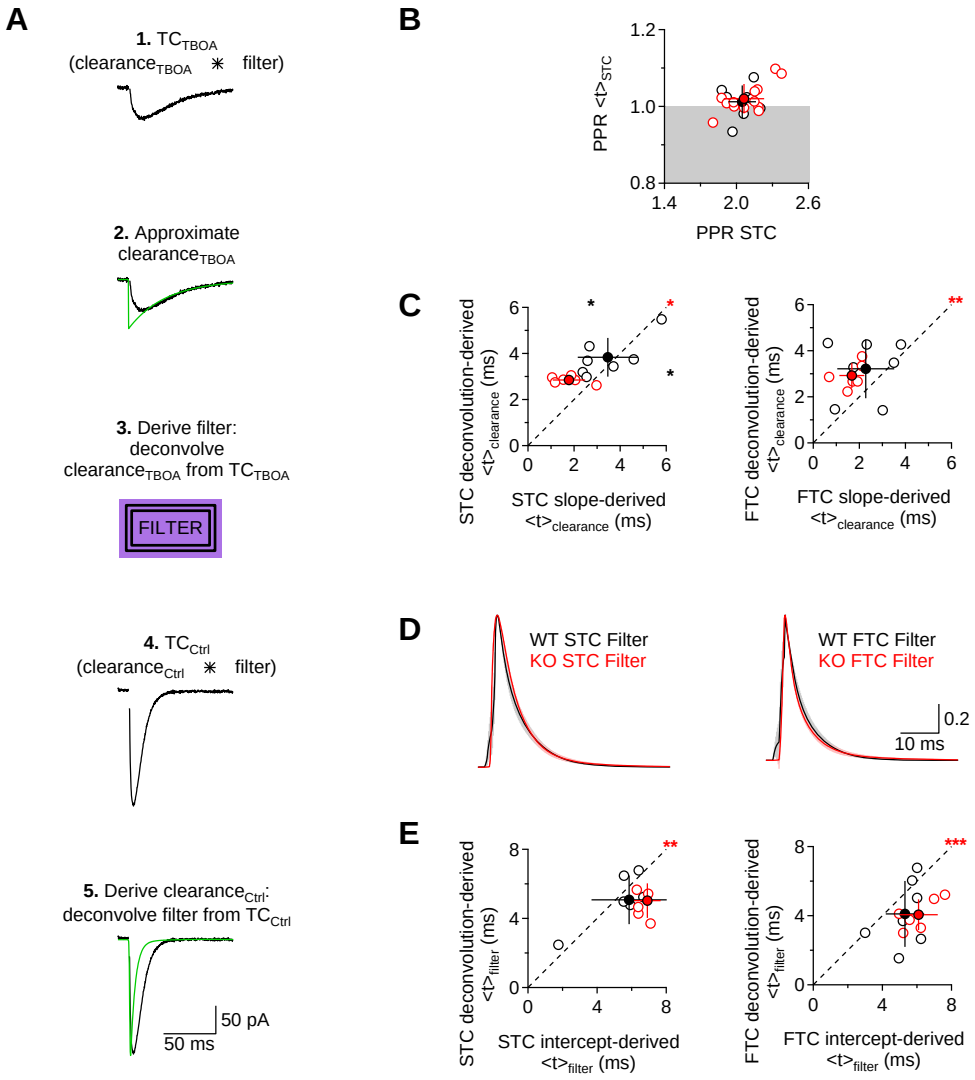

Supplementary Figure 7

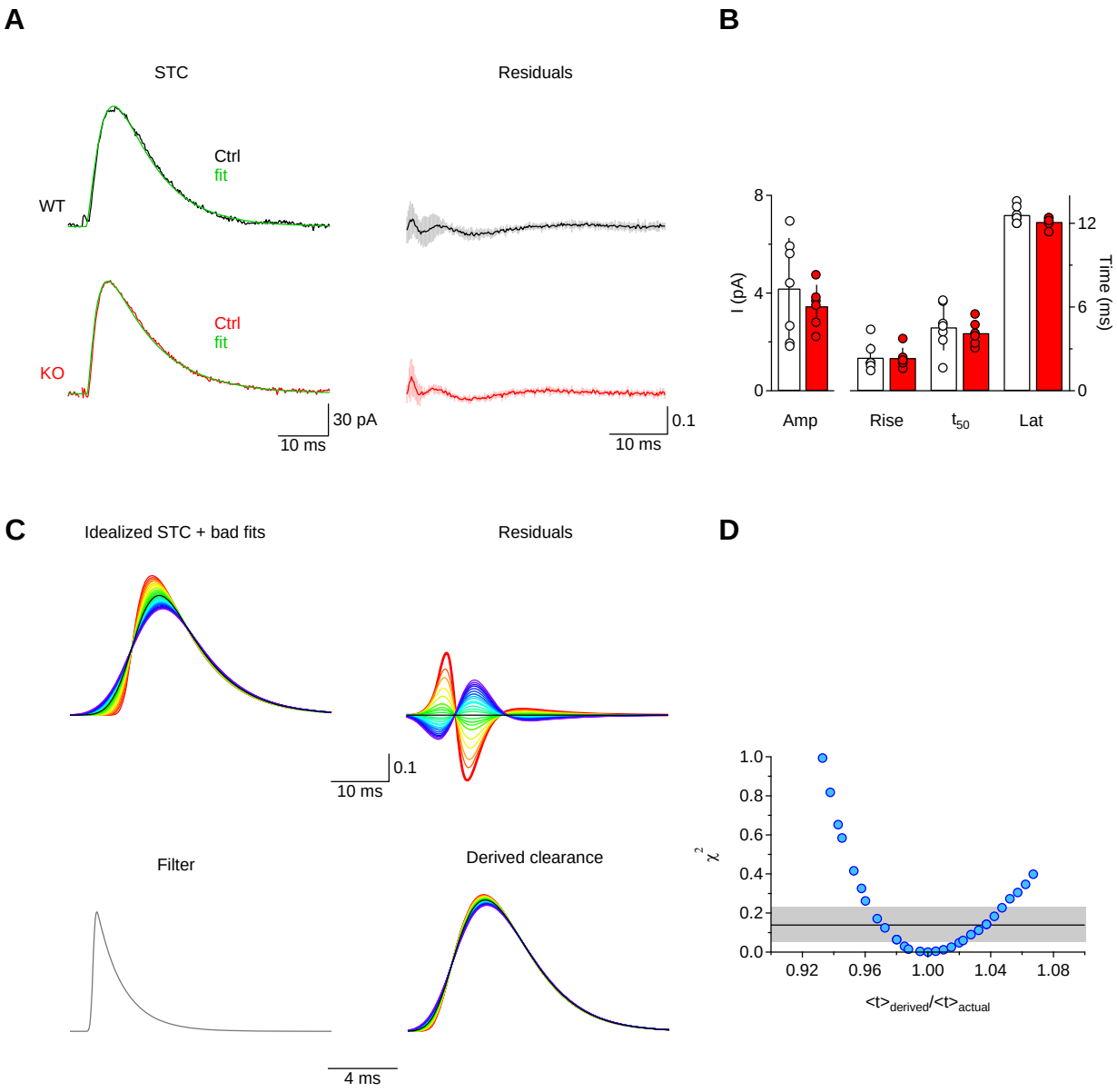

Supplementary Figure 8

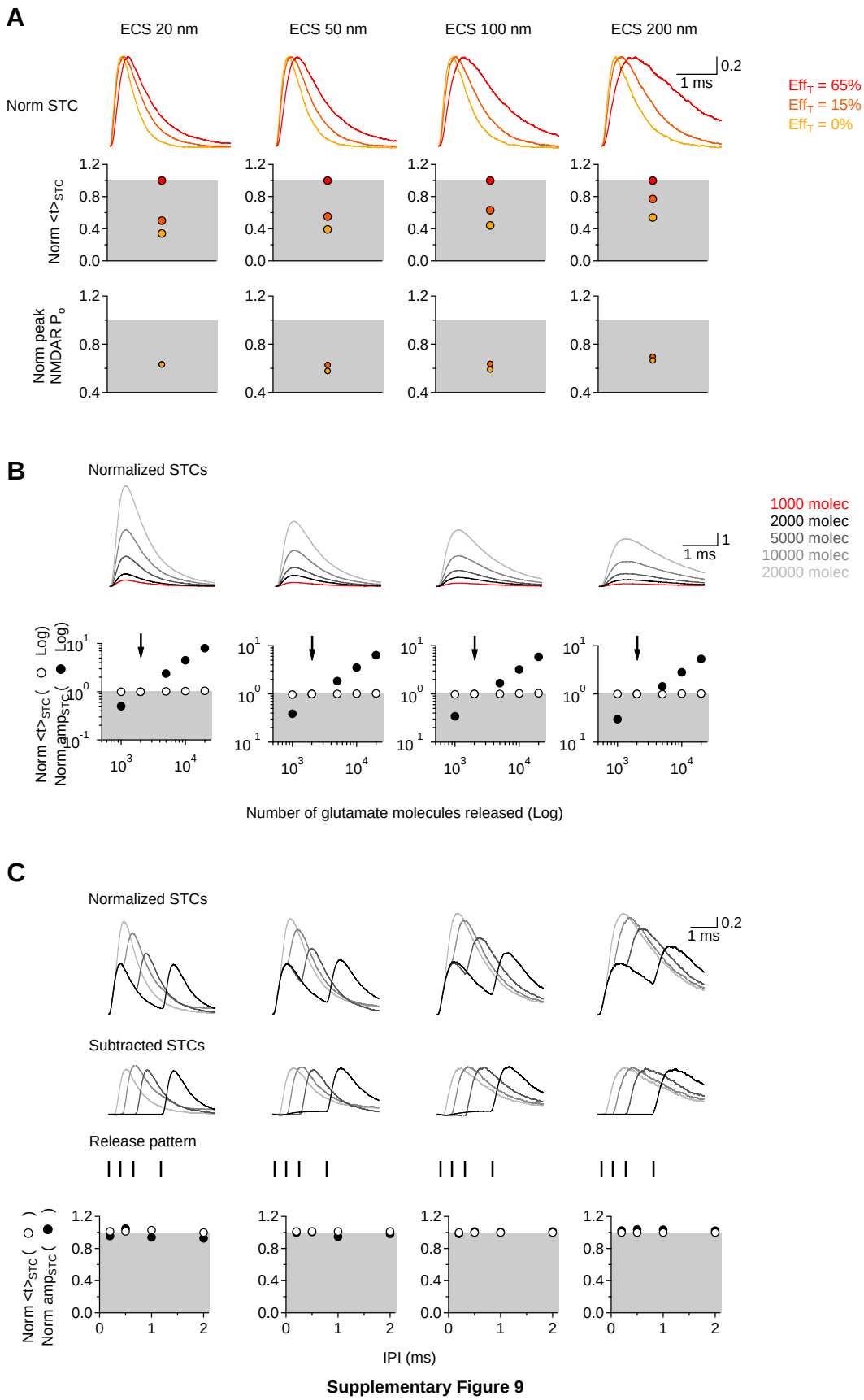

Supplementary Figure 9